

Article

Solidification Mechanism and Strength Characteristics of Alkali-Activated Tannery Sludge–Slag Geopolymer

Shoukai Chen ^{1,2,3}, Peidong Duan ¹, Mengdie Zhao ^{2,3,4,*}, Haibo Shi ¹ and Yajing Bie ^{1,2,3}

¹ School of Water Conservancy, North China University of Water Resources and Electric Power, Zhengzhou 450046, China; man200177@163.com (S.C.); 18736620265@163.com (P.D.); 17513360700@163.com (H.S.); yajing_bie@163.com (Y.B.)

² Henan Key Laboratory of Water Environment Simulation and Treatment, Zhengzhou 450045, China

³ Key Laboratory of Saving and Intensive Utilization of Water Resources in the Yellow River Basin, Zhengzhou 450045, China

⁴ College of Water Resource, North China University of Water Resources and Electric Power, Zhengzhou 450046, China

* Correspondence: zhaomengdie@ncwu.edu.cn

Abstract: The aim of this article is to reduce the environmental harm caused by industrial solid waste, specifically tannery sludge, and enable its reutilization. This study prepared an alkali-activated tannery sludge–slag solidification product (ATSSP) with high mechanical properties using blast furnace slag and tannery sludge as raw materials. The response surface methodology (RSM) was used to optimize the product mix ratio. The hydration mechanism and solidification method of ATSSP for Cr in tannery sludge were studied using X-ray diffraction (XRD), scanning electron microscope-energy dispersive spectrometer (SEM-EDS), and Fourier transform infrared reflection (FT-IR). The results indicate that the compressive strength regression model established through RSM has high accuracy and credibility. When the ratio of activator to binder is 0.2174, the alkali activation modulus is 1.02, and the water-to-cement ratio is 0.37; the 28 d compressive strength of ATSSP can reach 71.3 MPa. The sulfate in tannery sludge can promote the secondary hydration reaction of slag, and the generated hydrated calcium silicate and calcite greatly improve the strength of the ATSSP. The reducing substances contained in slag can reduce Cr (VI) in tannery sludge to Cr (III) in the form of uvarovite. The total Cr and Cr (VI) precipitation concentrations of the product are far less than the specification requirements.

Keywords: tannery sludge; slag; geopolymer; response surface methodology; heavy metal solidification



Citation: Chen, S.; Duan, P.; Zhao, M.; Shi, H.; Bie, Y. Solidification Mechanism and Strength Characteristics of Alkali-Activated Tannery Sludge–Slag Geopolymer. *Buildings* **2024**, *14*, 1060. <https://doi.org/10.3390/buildings14041060>

Academic Editor: Jan Fořt

Received: 29 February 2024

Revised: 31 March 2024

Accepted: 6 April 2024

Published: 10 April 2024



Copyright: © 2024 by the authors. Licensee MDPI, Basel, Switzerland. This article is an open access article distributed under the terms and conditions of the Creative Commons Attribution (CC BY) license (<https://creativecommons.org/licenses/by/4.0/>).

1. Introduction

Currently, the construction sector accounts for 30% of global greenhouse gas emissions [1,2], while mining and mineral processing operations contribute between 4% and 7% of global greenhouse gas emissions [3]. Both sectors face significant pressure to reduce their emissions. Additionally, the world faces widespread energy and resource scarcity, as well as environmental pollution problems resulting from the annual increase in various industrial waste. The rational utilization of solid waste in the construction industry can help reduce the extraction and consumption of new resources to alleviate resource scarcity, while also reducing environmental pollution and promoting sustainable development [4].

Slag is an industrial waste generated through high-temperature processing in processes such as metallurgy and energy production. The long-term stockpiling of slag can occupy a significant amount of land, impacting the effective utilization of land resources. Furthermore, the soluble components of slag may infiltrate downwards from the surface with water, thereby contaminating soil and water systems, leading to soil acidification, alkalinization, and hardening, as well as polluting water sources and human health [5]. However,

slag contains a large amount of oxides of Ca, Si, Al, Mg, and Fe, along with small amounts of sulfides. This unique composition enables slag to exhibit potential cementitious activity under specific conditions, which makes slag highly valuable for reuse in the construction industry [6].

On the other hand, China is one of the major leather production centers in the world. Tannery sludge comes from activated sludge produced in the process of tannery wastewater treatment. The composition of tannery sludge is complex, containing 20–30% inorganic substances, such as Si, Al, Fe, and Ca, but containing high concentrations of heavy metal Cr ions [7]. Traditional tannery sludge treatment methods are mainly landfill and incineration. If it cannot be well treated, it will cause certain pollution to soil and water resources [8] and even endanger human health [9,10]. Therefore, many scholars propose to treat tannery sludge with fixed/stable methods for resource reuse. Basegio et al. [11] used tannery sludge and clay as raw materials to synthesize ceramics and believe that this material can be used as bricks in the construction industry. Filibeli et al. [12] combined tannery sludge mixed with cement, sand, and fly ash and maintained it for 28 d. The strength of the cured body could reach the requirements of filler material. Jin et al. [13] synthesized tannery sludge with metakaolin as a curing agent, and the cured product had good resistance to high temperature, acid and alkali, and acid rain erosion. Amin et al. [14] used 10% sludge for the preparation of clay roof tiles and showed that the dry shrinkage and raw strength of the tiles decreased with the addition of waste. However, the problem of Cr ion exudation must be solved in the material utilization of tannery sludge. Ivanov et al. [15] studied the solidification effect of Portland cement on Cr (VI). The results showed that the hydration product C-S-H of Portland cement could not cure Cr (VI) well, and it also needed to add a reductant, which increased the cost of waste treatment. In contrast, geopolymer is a better choice for the treatment of hazardous waste [16].

Currently, numerous scholars are attempting to utilize industrial waste in the preparation of alkali-activated cementitious materials and geopolymers. Prasittisopin et al. [17,18] examined the modification effects of alkaline solutions on a mixed cementitious system containing rice husk ash, finding that the setting speed of the cementitious system is accelerated after alkali activation, leading to higher early compressive strengths and improved modification effects. Odimegwu et al. [19] utilized 50% alum sludge as a substitute for fly ash in the preparation of geopolymers, yielding products with good mechanical properties, with the peak compressive strength reaching approximately 80 MPa. Huang et al. [20] prepared alkali-activated mortars using urban solid waste incineration ash and slag and investigated the promotion of polymerization reactions by varying NaOH contents through microscopic analysis. The spatial structure of geopolymer is composed of a Si-O-Al polymer skeleton. Cross-linked Si-O tetrahedrons and Al-O tetrahedrons share all bridged oxygen atoms [21], in which the intermolecular force includes covalent bonds and ionic bonds, which have good mechanical properties [22]. In addition, geopolymers can form closed cage-like cavities by combining the “crystal-like” structure of their cyclic molecular chains to immobilize heavy metals or other contaminants in the cavities [23,24]. El-Eswed et al. [25] used kaolin/zeolite-based polymers for curing/stabilization of the heavy metals Pb, Cu, Cd, and Cr. The experimental results showed that Na⁺ and K⁺ are released from the geopolymer structure, while the heavy metal ions are effectively immobilized. Nikolić et al. [26] investigated the effect of fly ash activity and hydration product structure on the efficiency of curing Cr (VI) by alkali-excited fly ash geopolymer and concluded that the higher the strength of the prepared geopolymer, the higher the curing efficiency, indicating that physical curing action plays an important role in the curing of Cr (VI). Zhao et al. [27] used slag as a reducing agent to construct a self-heating system and were able to completely remove Cr (VI) from industrial wastewater. Galiano et al. [28] compared the effects of granulated blast furnace slag, kaolin, and metakaolin on the efficiency of fly ash geopolymer solidification of municipal solid waste incineration ash. The results showed that granulated blast furnace slag geopolymer had the highest Cr (VI) solidification rate, and the Cr (VI) leaching concentration was two orders of magnitude lower than that of Portland cement.

At the same time, alkali-activated slag material also shows many superior properties, such as high early strength, low permeability, better chemical corrosion resistance [29,30], fire resistance [31], and a stronger aggregate–substrate interface zone [32]. In conclusion, the preparation of geopolymer from alkali-activated slag can provide a solution to the problem of heavy metal pollution in the process of tannery sludge as building materials [33,34].

Based on this, this study aims to utilize tannery sludge in a resource-oriented manner. Utilizing tannery sludge and blast furnace slag particles (hereinafter referred to as slag) as raw materials, an alkali-activated tannery sludge–slag solidification product (hereinafter referred to as ATSSP) was prepared. Through response surface experiments, the optimal mixture ratio with alkali activators was explored, and its strength properties and chromium ion release concentration were tested. Microscopic tests were also conducted to investigate the hydration and solidification mechanisms of ATSSP, in order to promote the construction material utilization of tannery sludge.

2. Materials and Methods

2.1. Main Raw Materials

The slag was taken from S95 slag of Henan Zhengzhou Hengyuan New Materials Co, Zhengzhou, China. The FBT-9 fully automatic cement-specific surface area tester was used to determine its specific surface area was $450.03\text{m}^2/\text{kg}$, and the density was $2.93\text{g}/\text{cm}^3$. The main chemical composition of the slag was obtained by X-ray fluorescence (XRF) analysis, and the obtained results are given in Table 1. The main component of slag is CaO, which contains high levels of SiO_2 and Al_2O_3 . Under the action of alkaline activators, the silicon–oxygen bonds and aluminum–oxygen bonds are easily broken and recombined into stable calcium silicate and calcium aluminate minerals. Therefore, this slag is suitable for preparing geological polymers. According to the chemical composition of slag, the quality index of slag is calculated [35], and the results are shown in Table 2.

Table 1. Main chemical composition of slag.

Composition	CaO	SiO ₂	Al ₂ O ₃	Fe ₂ O ₃	MgO	SO ₃	TiO ₂	Na ₂ O	MnO
Percentage (%)	41.03	28.01	13.91	0.37	9.78	2.85	1.51	1.17	0.54

Table 2. Slag quality index.

Index	Alkalinity Coefficient	Activity Coefficient	Quality Coefficient	Water Stiffness
Number	1.21	0.50	2.15	2.31

According to Table 2, it can be seen that the slag used in this article has an alkalinity coefficient of $1.21 > 1$, which belongs to alkaline slag. The activity coefficient is $0.50 > 0.25$, which belongs to high activity slag. The quality coefficient is $2.15 > 1.2$, which belongs to high-quality slag. The water hardness coefficient is $2.31 > 1$; the content of active components in the slag is greater than the content of inactive components; the slag is of good quality and meets the requirements of this test.

Figure 1 shows the microscopic morphology of the slag. The main phases of the slag are CaCO_3 and SiO_2 , and the main composition is amorphous phase aluminosilicate [36]. The physical phase composition of the slag is mainly glassy. In addition, the particles in the slag are of different shapes with obvious angles, mainly in an amorphous state, and there is rarely a regular crystal structure. The particles are well-dispersed, although they are of different sizes. At the same time, it is found that the surface of slag produces many defects during the high temperature and rapid cooling water quenching process; the surface is the most unstable part of slag and the place where its hydration reaction is most likely to occur. When using alkaline activators to excite slag, it first causes the slag glass to dissociate into unstable structural units and then forms new cohesive structures through reaction. The depolymerization process includes the breaking process of Si–O–Si and Al–O–Si of two

covalent bonds under the polarization of high concentration of OH^- and alkali metal ions and then transforms into a large amount of silica–aluminum gel phase, and the gel phase accumulates to a certain degree to form a cohesive structure, leading to the formation of new phases and the development of a dense structure.

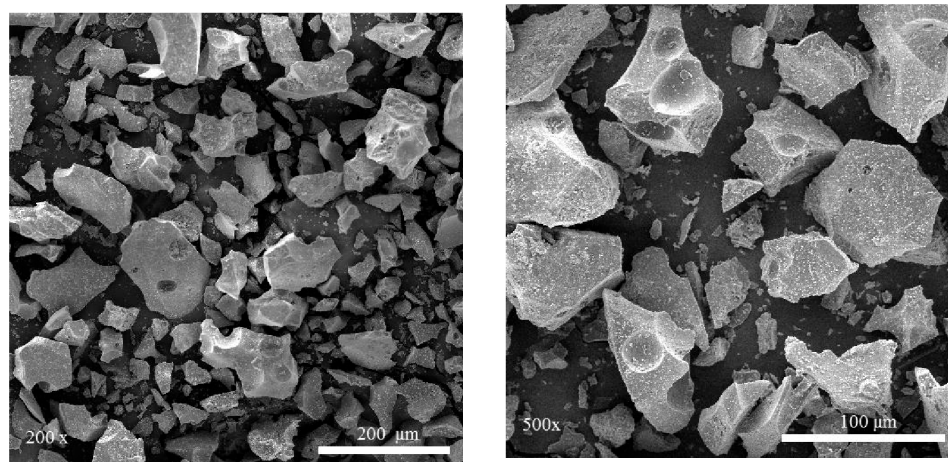


Figure 1. Scanning electron micrograph of slag.

Of note, the slag itself contains some low valence reducing sulfur, generally in the form of S^{2-} and elemental S [37], and with the continuous dissociative hydration of the slag, the reducing sulfur will also continuously enter the pore solution and hydration products. Eventually, the reducing sulfur inside the pore solution mainly exists in the form of S^{2-} and $\text{S}_2\text{O}_3^{2-}$, and the low valence S is useful for the solidification/stabilization of Cr (VI), which is beneficial.

Tannery sludge was obtained from a tannery wastewater treatment plant in Pingji County, Henan Province, China. Table 3 shows the main components of the sludge based on XRF analysis, and Figure 2 shows the SEM image of tannery sludge. From Table 3, there are more CaO, SO_3 , and some other metal oxides in the tannery sludge, which are mainly generated by the addition of quicklime and sulfate in the tannery sludge tanning precipitation process. The abundance of calcium helps to compensate for the deficiency of calcium ions in the sludge, thus avoiding the phenomenon of reduced strength caused by the excess generation of indeterminate substances from the remaining silica aluminates caused by a single alkali excitation of the sludge. Sulfate within tannery sludge regulates the coagulation time of ATSSP and generates calcium alumina to consume Ca^{2+} and promote slag depolymerization [38]. According to the chemical composition of tannery sludge, the quality indexes of tannery sludge are calculated, and the results are given in Table 4.

Table 3. Main chemical composition of tannery sludge.

Composition	CaO	SiO ₂	Al ₂ O ₃	Fe ₂ O ₃	MgO	SO ₃	P ₂ O ₅	Na ₂ O	Cr ₂ O ₃
Percentage (%)	33.51	6.72	3.04	17.52	2.84	20.51	2.59	1.17	5.49

At the same time, the only harmful heavy metal in the tannery sludge is Cr ion, so it is necessary to determine the leaching concentration of chromium ion in the tannery sludge to ensure the safety of ATSSP. After testing, the Cr (VI) leaching concentration of tannery sludge used in this study was tested to be 0.317 mg/L, and the total Cr content was 78.60 mg/L.

To ensure the physical properties of ATSSP and make tannery sludge react with slag rapidly, tannery sludge was pretreated in this study. Firstly, a crusher was used to crush the filtered and dehydrated sludge board into small particles and remove the obvious animal fur tissue. Then the powder mill was run for 1 min to crush the granular sludge

into powder and pass it through a 0.15 mm sieve. Finally, the screened sludge was put into an oven for drying treatment before use.

The particle size distribution curves of slag and tannery sludge used in this article are shown in Figure 3.

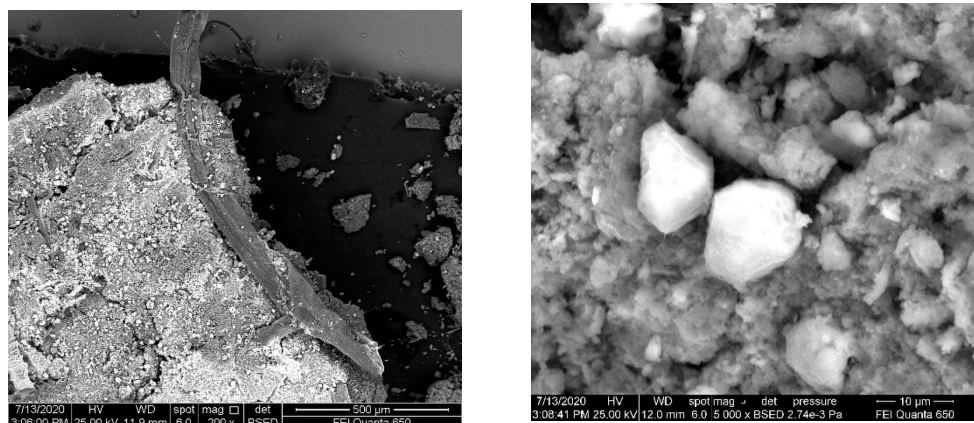


Figure 2. Scanning electron micrograph of tannery sludge.

Table 4. Tannery sludge quality index.

Index	Alkalinity Coefficient	Activity Coefficient	Quality Coefficient	Water Stiffness
Number	3.72	0.45	5.24	5.86

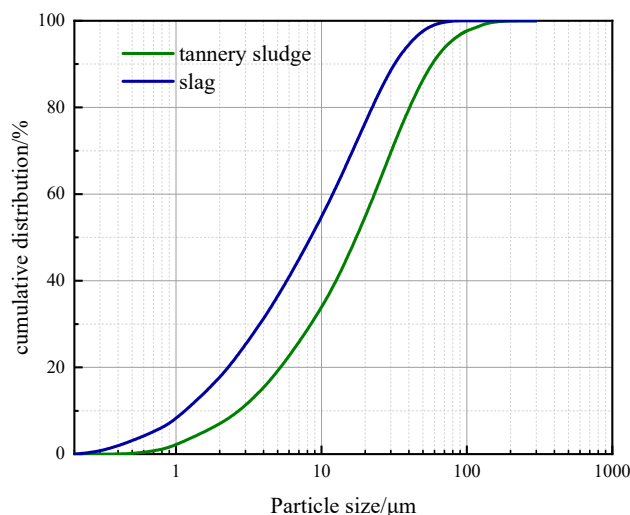


Figure 3. Particle size distribution curves of slag and tannery sludge.

The alkali exciter was prepared with water glass with an initial modulus of 3.3 and a water content of 64.16% together with solid NaOH of 95% purity.

2.2. Test Preparation and Process Flow

2.2.1. Single-Factor Test Validation at an Early Age

The composite geopolymer is synthesized from a blend of various raw materials or multiple geopolymers, presenting a more complex composition and structure compared to single geopolymers. Currently, there are no studies on the preparation of composite geopolymers by combining tannery sludge with slag. To achieve composite geopolymer materials with superior mechanical properties, this study first conducts early-stage single-factor tests to validate the feasibility and strength patterns of ATSSP and to determine the appropriate ranges for the three variables: activator modulus, activator–binder ratio, and

water–binder ratio, for subsequent response surface methodology (RSM) experimental design. Where the activator modulus is the ratio of the amount of SiO_2 to Na_2O in its component sodium water glass, and the value is adjusted by adding NaOH and water to the water glass; the activator–binder ratio is the ratio of the mass of alkali activator to binding materials (slag, tannery sludge); the water–binder ratio is the mass ratio of water to the binding materials. Figure 4 shows the effect law of the alkali-activation modulus, excitation gel ratio, and water–binder ratio on the early compressive strength of the ATSSP. From the single-factor test, the three factors have a greater influence on the early strength of the ATSSP. The lowest value of the 7 d compressive strength is 29.8 MPa, and the maximum value is approximately 61.0 MPa. The forming quality and apparent morphology of the specimens are good, which indicates that the ATSSP has good glue material characteristics.

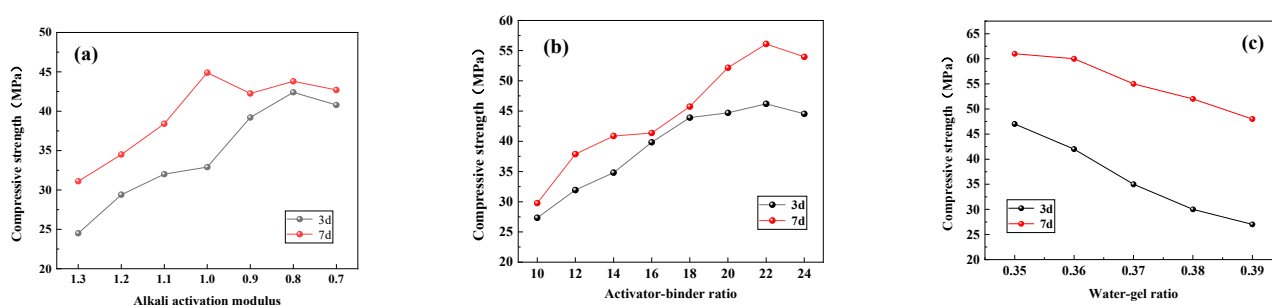


Figure 4. Research on factors influencing the compressive strength of ATSSP: (a) alkali-activation modulus, (b) activator–binder ratio, and (c) water–gel ratio.

With the designed activator–binder ratio of 15% and water–binder ratio of 0.35, the variation in the ATSSP strength was studied when the alkali activation modulus ranged from 0.7 to 1.3. When the alkali activation modulus is higher, the silica content is higher and the water glass is more viscous; conversely, the lower the alkali activation modulus, the higher the alkali content, and the greater the excitation effect on the silica–alumina material. As seen from the obtained results, with the increase in the alkali excitation model, the early compressive strength of the ATSSP shows a trend of first increasing and then decreasing; when the value is 1, the strength of the ATSSP reaches the maximum, 44.9 MPa. The alkali-activation modulus changes more obviously at 0.9 and 1.1. Considering the interaction between factors, the reasonable range of the alkali excitation model is 0.8–1.2.

A water–gel ratio of 0.35 and an alkali-activation modulus of 1.0 were designed to study the variation in the ATSSP strength when the activator–binder ratio was 10–24%. The alkali content (Na_2O) of the equivalent alkali activator increases as the excitation glue ratio increases. From the obtained results, the early compressive strength of the ATSSP reaches a maximum at 22%, which is 56.1 MPa. The reasonable range of the activator–binder ratio is 20–24%.

With an alkali-activation modulus of 1.0 and a radical glue ratio of 22%, the variation in the ATSSP strength was studied from 0.35 to 0.39. From the obtained results, the compressive strength increases with the lower water–binder ratio, and the variation law is approximately linear, which is basically consistent with the law of cement-based materials. When the water–binder ratio is 0.35, the early compressive strength of the ATSSP is the largest, 47 MPa at 3 d and 61.6 MPa at 7 d; when the water–binder ratio is 0.39, the compressive strength is the lowest, 27 MPa at 3 d and 48 MPa at 7 d. When the water–binder ratio is too large, the concentration of exciter and OH^- decreases, the reaction rate decreases, and the excitation effect on the slag ATSSP is weakened, while the ATSSP pore space increases and strength decreases [39,40]. Considering that the water–colloid ratio directly affects the alkali-activation modulus and the role of the activator–binder ratio, the range of the water–colloid ratio was selected as 0.35–0.39.

2.2.2. Process Flow

From the abovementioned single-factor test, the reasonable values of three variables, namely, the activator–binder ratio, alkali-activation modulus, and water–binder ratio, were determined to be in the ranges of 18–24%, 0.8–1.2%, and 0.35–0.39, respectively.

Based on this, the Box–Behnken model in response surface analysis (RSM) was used for the experimental design, and a single-factor asymptotic analysis was conducted with compressive strength as the response value. Table 5 shows the test factor codes. For the convenience of analysis, the activator–binder ratio, alkali-activation modulus, and water–binder ratio are indicated by the coded values A, B, and C, respectively. The high and low coding levels are denoted by 1, 0, and -1 , respectively.

Table 5. Coding and level of test-independent variable factors.

Factors	Code Value	Coding Level		
		-1	0	1
Activator–binder ratio	A	18%	21%	24%
Alkali-activation modulus	B	0.8	1	1.2
Water–binder ratio	C	0.35	0.37	0.39

According to the abovementioned design results, the ATSSP was prepared, and the experimental operation flow is shown in Figure 5.

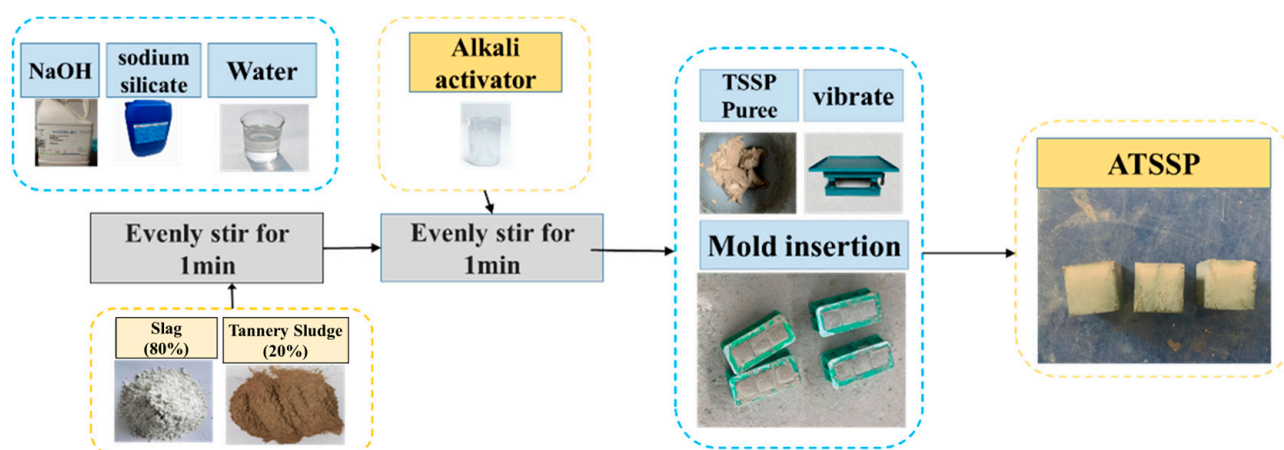


Figure 5. Experimental diagram of the ATSSP.

(1) Blend the alkali exciter required for the test proportion 1 d in advance and seal it for natural cooling to avoid the effect of rapid temperature rise of caustic soda in contact with water.

(2) Weigh the slag (80%) and tannery sludge (20%) powder according to the mass ratio and pour them into the stirring pot with slow stirring for approximately 60 s to make their distribution completely uniform.

(3) Slowly inject the alkali exciter configured in step 1 into the mixing pot (keep the mixing pot stirring at a slow speed during the period) and stir it rapidly for 60 s after the injection is completed to make it fully mixed.

(4) Pour the homogeneous slurry into the triple touch (size 40 mm × 40 mm × 40 mm) and use the cementitious sand vibrating table to vibrate it while entering the mold to ensure that the air is discharged when the slurry is in the mold and to avoid delamination of the test block due to early setting of the slurry.

(5) Demold the test block after 24 h of natural curing and then put it into a constant temperature and humidity curing box for curing until reaching the specified age.

(6) After curing, the compressive strength was tested; the specimens for microscopic analysis were terminated with anhydrous ethanol for hydration to be measured.

2.3. Test Method

The ATSSP compressive strength test was performed using 40 mm × 40 mm × 40 mm cubic specimens, three in each group. The electro-hydraulic servo pressure testing machine is used for the test. The loading rate is set to 600 N/s.

X-ray fluorescence (XRF) is used to determine the types and contents of chemical elements in samples.

X-ray diffraction (XRD) was used to test the type of reaction products in the cured body of tannery sludge.

Scanning electron microscopy (SEM) was used to observe the microscopic morphology of the raw materials and reaction products of tannery sludge–slag based composite geopolymers, which is also equipped with an EDS energy spectrometer.

FT-IR analysis can determine the functional groups or chemical bonds or vibrational changes contained in the specimen, characterize the substance, quantify it, study the reaction process, and contribute to a deep understanding of the mechanism of alkali-excited slag curing/stabilization of tannery sludge.

The total chromium leaching concentration test method refers to the “Solid waste-Extraction procedure for leaching toxicity. Sulphuric acid & nitric acid method” [41]; the hexavalent chromium leaching concentration test method refers to the “Solid waste-Determination of chromium (VI)-1,5-Diphenylcarbohydrazide spectrophotometric method” [42]. In this study, leachate was digested using the US EPA 3010a (HNO₃-HCl digestion system) method.

This study used the Box–Behnken design (BBD) model in the Design-Expert 13 software for RSM. The compressive strength of the material was used as the response variable, and the activator–binder ratio, alkali-activation modulus, and water–binder ratio were used as independent variables, with their value ranges including low, medium, and high values. The experimental design table was followed for experimental operation, and the response variable values for each test point were recorded. The experimental data were entered into the Design-Expert 13 software. An appropriate model was selected to describe the relationship between the independent variables and the response variables. The software will automatically perform statistical analysis based on the experimental data, including significance testing of the model, detection of non-fit items, and correlation testing. The relationship between variables can be visually understood through the graphical display of the model (such as the response surface plot and contour plot). Finally, based on the predicted results of the model, the optimal operating conditions or parameter combinations can be determined.

3. Results and Discussion

3.1. Experimental Results and Model Selection

For the research of building materials, most of the studies focus on the influence of a single variable on its performance, while there are few studies on the interaction of multiple factors. Response surface methodology (RSM) can intuitively obtain the influence of multiple factors on their performance through response surface models and effectively predict the response results. RSM has the advantages of fewer experimental times, shorter cycle time, high accuracy, and wide applicability. At the same time, it overcomes the defects that orthogonal experiments cannot obtain the relationship expression between experimental factors and response targets in the specified entire region and cannot provide intuitive graphics. In addition, the RSM model is a method that effectively combines experimental design and mathematical modeling and optimizes the results [43]. It adopts fractional factorial experiments and, through experiments on representative local test points, regresses and fits the data of representative test points to obtain the functional relationship between factors and results in the global range. Through optimization, it can

obtain the optimal level value of each factor on the response results [30]. Therefore, it plays an increasingly important role in solving practical application problems.

Table 6 shows the measured results of the compressive strength of the ATSSP based on the RSM method. It can be seen that when $A = 21\%$, $B = 1.0$, and $C = 0.37$, the 28 d compressive strength of ATSSP is the highest at 72.4 MPa. In addition, it can be seen from the obtained results of sequences 13 to 17 that the measured 7 d and 28 d compressive strengths are more stable under the same variable conditions, and the variation is less than 10%, which can be used for subsequent analysis.

Table 6. Test values of the mechanical properties of the ATSSP.

Specimen	Factor			Compressive Strength/MPa	
	A	B	C	7 d	28 d
1	18%	0.8	0.37	45.0	56.8
2	24%	0.8	0.37	52.1	58.5
3	18%	1.2	0.37	43.8	61.6
4	24%	1.2	0.37	50.2	58.7
5	18%	1	0.35	46.0	52.5
6	24%	1	0.35	56.7	56.8
7	18%	1	0.39	45.3	57.1
8	24%	1	0.39	48.0	62.9
9	21%	0.8	0.35	45.4	54.7
10	21%	1.2	0.35	45.6	52.3
11	21%	0.8	0.39	46.1	54.6
12	21%	1.2	0.39	44.3	62.8
13	21%	1	0.37	52.7	72.4
14	21%	1	0.37	52.1	66.5
15	21%	1	0.37	53.5	71.1
16	21%	1	0.37	54.3	70.6
17	21%	1	0.37	54.4	69.8

With the help of Design-Expert software, linear, two-factor (2FI), quadratic, and cubic polynomial models were used to analyze the relationship between the ATSSP compressive strength test values and the activator–binder ratio, alkali-activation modulus, and water–binder ratio and output the hypothesis test p -value and misfit term p -value. The corrected values of the correlation coefficient R^2 and predicted values were output. The calculated results are given in Table 7. As seen from the table, among the four models, the hypothesis test p -value of the quadratic polynomial model is the smallest, 0.0001, which is less than 0.01 and very significant, while the p -value of the misfit term is the largest, much larger than 0.05 and the least significant, and the other three models have the opposite results. In addition, the difference between the R^2 corrected and predicted values of the quadratic polynomial model is less than 0.2. Therefore, the quadratic polynomial model is the most reasonable for analyzing the compressive strength properties of the ATSSP.

Table 7. Comprehensive analysis results of compressive strength by various models.

Source	p -Value				R^2			
	Sequential		Lack of Fit		Adjusted		Predicted	
	7 d	28 d	7 d	28 d	7 d	28 d	7 d	28 d
Linear	0.109	0.666	0.005	0.011	0.215	−0.096	−0.019	−0.311
2FI	0.818	0.905	0.003	0.006	0.0669	−0.350	−0.688	−1.039
Quadratic	0.0004	0.0001	0.126	0.449	0.886	0.888	0.399	0.606
Cubic	0.126	0.449	/	/	0.946	0.893	/	/

3.2. Regression Equation and Merit Search Test

Based on the quadratic polynomial model, the quadratic multiple regression equations for 7 d compressive strength (Y1) and 28 d compressive strength (Y2) were established as follows:

$$S_{7d} = 53.4 + 3.4A - 0.6B - 0.2C - 0.2AB - 1.9AC - 0.5BC - 1.1A^2 - 0.6B^2 - 3.4B^2 - 2.3A^2C \quad (1)$$

$$S_{28d} = 70.1 + 2.5A + 1.4B + 2.6C - 1.2AB + 0.4AC + 2.7BC - 5.0A^2 - 6.2B^2 - 7.8B^2 - 2.8AB^2 \quad (2)$$

Table 8 shows the obtained results of the plausibility test analysis of the compressive strength model of the ATSSP, and Figure 6 shows the comparison between the predicted and tested values of the compressive strength. As seen from the table, the multiple regression coefficients R^2 of the predicted and measured values of the 7 d and 28 d compressive strengths of the ATSSP were 0.9852 and 0.973, respectively, and the differences between the corrected and predicted R^2 values were 0.031 and 0.025, respectively, and the coefficients of variation (C.V. %) were 1.74% and 2.96%, respectively, and the signal-to-noise ratios (Adeq Precision) were 18.51 and 12.30, respectively. This indicates that the results of the regression equations in Equations (1) and (2) are calculated with less dispersion, higher confidence and accuracy, and more reliability and can be used for the prediction and analysis of the compressive strength of the ATSSP.

Table 8. Results of model plausibility test analysis.

Model	Std. Dev.	Mean	R^2	Adj R^2	Pred R^2	Press	C.V.%	Adeq Precision
S_{7d}	0.853	49.11	0.985	0.960	0.929	34.26	1.74	18.51
S_{28d}	1.81	61.16	0.973	0.928	0.953	362.45	2.96	12.30

Note: The closeness of the correlation coefficient R^2 to 1 and the difference between its correction value and the predicted value are used to verify the fit of the regression equation, which is less than 0.2 as a good fit; the smaller is the coefficient of variation (C.V.) (less than 10%), the higher is the accuracy of the data; the signal-to-noise ratio (Adeq Precision) is greater than 4, which indicates that the model can be run in the design space of this experiment. Std. Dev. is the standard deviation; Press is the predicted residual sum of squares.

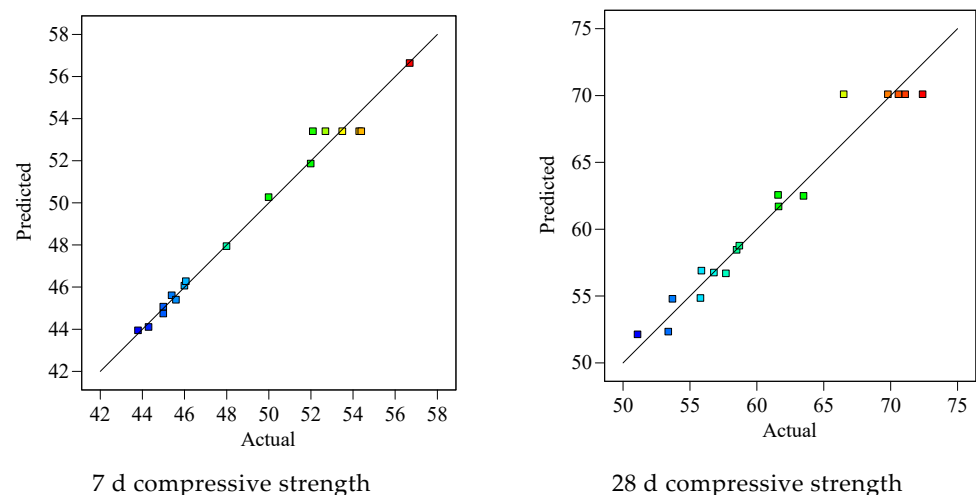


Figure 6. Comparison of actual and predicted values.

3.3. Multifactor Interaction Analysis

Figures 7 and 8 show the obtained results of the factor interactions (surface and contour plots) for the 7 d and 28 d compressive strength response surfaces of the ATSSP, respectively. Figure 7a–c show that the two-factor interaction surfaces show obvious steep slopes, indicating that A, B, and C have more obvious effects on S_{7d} (7 d compressive

strength); Figure 7d,e show that the contour density along factor A (activator–binder ratio) moves toward the peak and is significantly higher than that along factors B (alkali-activation modulus) and C (water–binder ratio), which indicates that A has the largest contribution to Y1. This ANOVA result is consistent; as shown by the contour plots in Figure 7d,f, S_{7d} achieved the maximum value when B was 1. The interaction of AC is much larger than that of AB and BC.

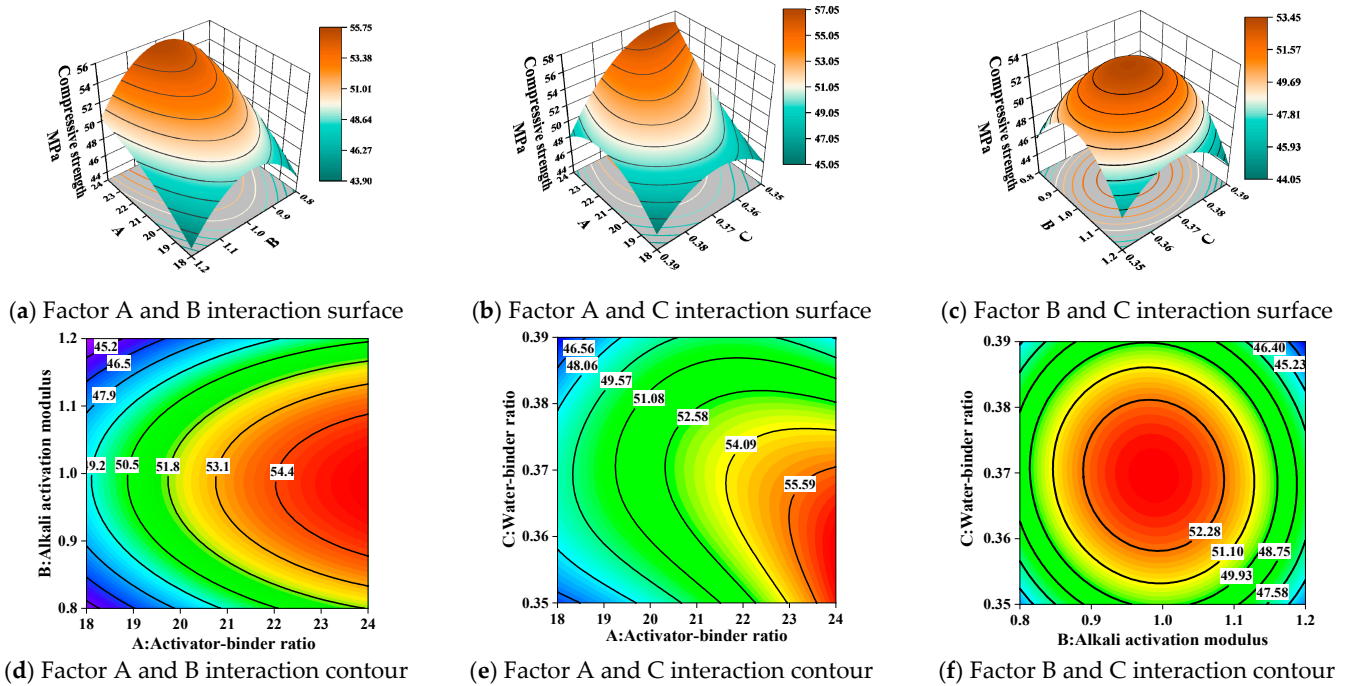


Figure 7. Influence analysis of the strength response surface factor at 7 d.

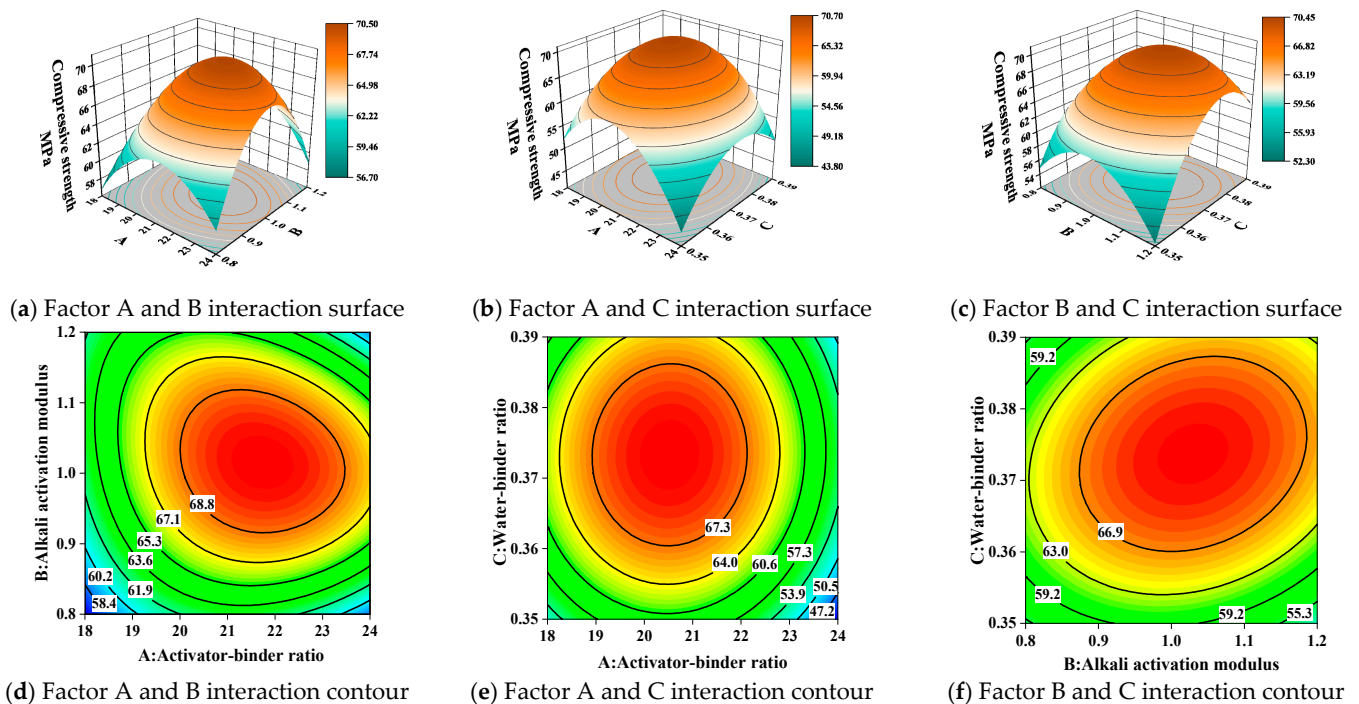


Figure 8. Influence analysis of the strength response surface factor at 28 d.

As seen in Figure 8a–c, the model opens downward, that is, the test results have a maximum value, and the maximum value falls within the test range, indicating that the significance test takes a reasonable and valid range. The contour plot of Figure 8f is elliptical in shape, and combined with the ANOVA, it can be seen that the interaction of BC has the greatest effect on S_{28d} (28 d compressive strength). The changes in both B and C will affect the alkali concentration of the ATSSP test blocks, i.e., the regulation of B relies on sodium hydroxide, and the size of C directly affects the content of alkali within the unit of water, which will have an important effect on the hydration of the ATSSP. In contrast, the interaction between AB and AC is relatively weaker than the contribution of BC to S_{28d} .

In addition, comparing Figures 7 and 8, it is found that A has a greater effect on the early strength of the ATSSP, indicating that the early strength mainly relies on the silicate within the alkali exciter combined with calcium ions to generate C-S-H gels to provide strength [44]. Larger values of the compressive strength of the ATSSP at both ages can be achieved for B of 1. In addition, a low C is beneficial to the early strength formation of the ATSSP, but an appropriate increase in the C value can appropriately reduce the alkali concentration of the liquid phase in the early stage and reduce the phenomenon that the generated C-S-H-wrapped slag hinders later hydration due to the high alkali concentration.

Design-Expert software has a numerical optimization module, which can select the desired target for each variable and response value when performing numerical optimization. The 28 d compressive strength is selected as the maximum value, and the best values of the variables are obtained, as detailed in Table 9. From the table, we can see that A is 21.74%, B is 1.02, C is 0.37, the measured value is 71.30 MPa, and the predicted value is 70.71 MPa; the relative error between the measured value (71.30 MPa) and the predicted value (70.71 MPa) is only 0.82%. The desired function value is 0.939, which indicates that the predicted value has good reliability.

Table 9. Comparison of predicted values and test values after parameter optimization.

A	B	C	7 d Compressive Strength			28 d Compressive Strength			Desirability
			Predicted /MPa	Test /MPa	D/%	Predicted /MPa	Test /MPa	D/%	
21.74	1.02	0.37	53.77	52.6	2.22	70.71	71.30	0.82	0.939

Note: D is the relative error between the predicted value and the measured value.

Table 10 shows the obtained results of the heavy metal Cr precipitation test of the ATSSP after the optimized ratio. The obtained results show that the total chromium precipitation concentration of ATSSP is 1 mg/L and the Cr (VI) precipitation concentration is 0.05 mg/L, both of which are much smaller than the national hazardous waste toxicity leaching standard [45].

Table 10. Cr precipitation test of the ATSSP.

Indicator Name	Total Chromium	Cr (VI)
Before curing (mg/L)	78.60 mg/L	0.32 mg/L
After curing (mg/L)	1 mg/L	0.05 mg/L
Leaching rate	1.27%	15.77%
Normative limit value	15 mg/L	5 mg/L

3.4. Analysis of the Hydration Mechanism

3.4.1. Analysis of Physical Phases

Figure 9 shows the XRD patterns of the preferred fit ratio ATSSP at different ages. The main hydration products of ATSSP are C-S-H, where C-S-H is the free calcium oxide from slag, and calcium sulfate from tannery sludge reacted with alkaline exciter to produce calcium silicate hydrate. Calcium oxide and calcium sulfate from tannery sludge reacted

with the silica–alumina component to produce hydrated calcium silicate in the presence of alkaline exciter, which is similar to the results of previous studies on the excitation of sulfate on slag [46], indicating a facilitative effect of tannery sludge on the hydration reaction of ATSSP. In addition, the diffraction peaks of the C-S-H gel and calcite (CaCO_3) overlap, and calcite is formed due to the interaction of partial hydration products with atmospheric CO_2 [47]. The abovementioned figure also shows a quartz phase (quartz), which indicates a crystalline phase with residual raw material, and the intensity of the diffraction peaks gradually decreases with the age of conservation, indicating that the glassy phase of ATSSP continuously depolymerizes and generates new C-S-H gels with the age of conservation, resulting in an increase in strength. In addition, the intensity of the diffraction peak of calcium–aluminum yellow feldspar (Gehlenite) basically does not change, which indicates that the physical phase of calcium–aluminum yellow feldspar is relatively stable and does not have hydration reaction activity.

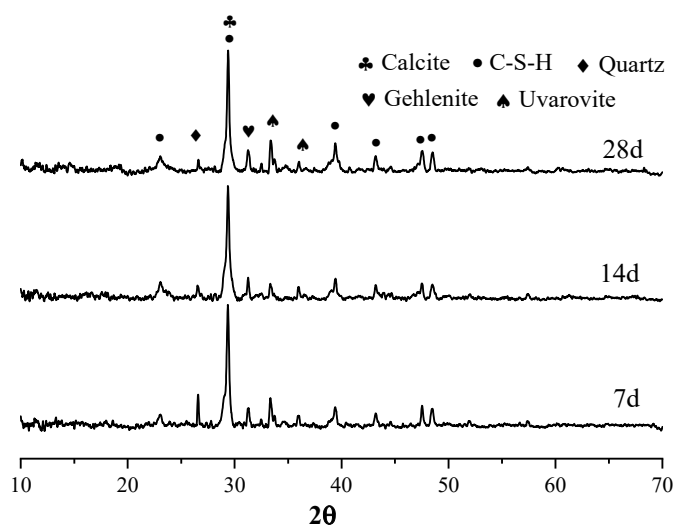


Figure 9. XRD patterns of the optimum mix proportion of solidified product at different ages.

Of note, the diffraction peaks of uvarovite ($\text{Ca}_3\text{Cr}_2[\text{SiO}_4]_3$) are present in the ATSSP at all ages in Figure 9, which is a mineral generated by the reaction of slag with the heavy metal cation Cr (III) of tannery sludge that replaces Ca^{2+} during the hydration reaction. This indicates that the ATSSP achieved the solidification of Cr (III). This shows that the ATSSP can not only physically stabilize the tannery sludge with a three-dimensional mesh structure but can also chemically stabilize the sludge by forming stable minerals from Cr (III). Overall, the intensity of the diffraction peaks of the ATSSP hydration products increased with age, indicating that the mechanical properties and solidification/stabilization ability of the ATSSP were also gradually enhanced.

3.4.2. Micromorphology

Figure 10 shows the microstructure of the ATSSP at 7 and 28 d for the preferred mix ratio. From the figure, it can be seen that at 7 d, there are still unhydrated slag particles on the surface of the ATSSP, and the surface layer has formed loose C-S-H gel and continuously accumulates on the surface to form the hydration product “wrapping layer”, and the large number of cracks found in the figure is the “wrapping layer”. The large number of cracks found in the figure is the rupture of the “inclusions” under the action of the crystallization pressure of the hydration products and the osmotic pressure of the solution through the hydration products. By 28 d, the new hydration products continue to precipitate in large quantities so that the “wrapping layer” can then heal, and the liquid phase ions have difficulty passing through the outer layer of hydration products, resulting in a slower hydration process. The final hydration process is controlled by the diffusion process of reactants through the dense hydration product layer, thus forming a

dense three-dimensional cage-like structure. This structure can completely sequester the tannery sludge particles wrapped by the hydration products in the early stage within the gel. As the age increases, the Ca-Si ratio decreases from 1.265 to 1.064, and the C-S-H gel in the ATSSP incorporates more Al, which replaces Si in the Si-O tetrahedra at the bridge oxygen position in the C-S-H gel. Hydration becomes more adequate. EDS point sweep analysis of the selected microregion was performed to obtain the elemental composition of the region (point), as detailed in Figure 10g–i. The selected area 1 (Selected Area 1) is a white bulk structure of the 7 d hydration product, which is mainly composed of O, Si, S, Ca, and a large number of other metal cations (such as Na, Al, Mg, Cr, and Fe). This indicates that the bulk is mainly composed of C-S-H, C(N)-A-S-H, and calcium alumina feldspar. Microspot sampling (EDS Spot 1) of the white flocculent gel revealed that the material was a C-S-H gel, in which a small amount of Cr was also found, indicating that some Cr replaced Ca^{2+} to form a stable mineral structure, which, combined with XRD (Figure 9) analysis, indicates that the material is calcium-chromium garnet ($\text{Ca}_3\text{Cr}_2[\text{SiO}_4]_3$). Heavy metal ions are dissolved into the hydration products or react with the hydration components to form precipitates. Due to its high specific surface area ($100\text{--}700\text{ m}^2/\text{g}$), heavy metals can be adsorbed on its surface first and then intervene in C-S-H+M-M-C-S-H or replace C-S-H+M- \rightarrow M-C-S-H+ Ca^{2+} . In addition, the analysis of the EDS energy spectrum of the 28 d hydration products revealed that only a small amount of S from the tannery sludge was present, and no Cr was found. This is thought to be due to the dense three-dimensional mesh structure that encapsulates and seals the cured products, further hindering the precipitation of heavy metals, thus achieving the effect of physical adsorption [25,48]. In addition to the curing effect, the inhibition of Cr (VI) leaching by reduction is also an important effect. The slag produced during the ironmaking process may contain small amounts of reducing substances such as Fe^{2+} and S^2 [46,49]. The Cr (VI) leaching concentration decreased from 0.317 mg/L to 0.05 mg/L before and after curing, and it is presumed that some of Cr (VI) was reduced to Cr (III) by the reducing substances in the slag. The following reaction occurred: $3\text{S}^{2-} + 8\text{CrO}_4^{2-} + 20\text{H}_2\text{O} = 3\text{SO}_4^{2-} + 8\text{Cr}^{3+} + 40\text{OH}^-$. The reduced Cr (III) is then more easily solidified.

3.4.3. FT-IR Analysis

Figure 11 shows the FTIR spectra of ATSSP at different ages. A review of the corresponding literature shows that the absorption band at wave number around 3450 cm^{-1} corresponds to the stretching vibration of $-\text{OH}$, while the absorption peaks at $1600\text{--}1700\text{ cm}^{-1}$ are produced by the bending vibration of H-O-H, both of which indicate the presence of some free and bound water in the sample, and the subsequent increase in peak intensity with age indicates the production of more hydration products; the absorption band near 1450 cm^{-1} is a stretching vibration of C=O, which is caused by the carbonization of the sample during the hydration process. The absorption peak appearing near 1000 cm^{-1} is the Si-O or Al-O bond asymmetric stretching vibration, which is a significant sign to identify C-(A)-S-H [50], and the peak shift is caused by the hydration product C-(A)-S-H gel being subjected to carbonation resulting in lower calcium content; about 460 cm^{-1} is the Si-O bond bending vibration peak in silica-oxygen tetrahedra [51]. The peak positions of C-S-H and silica-oxygen tetrahedra tended to move to higher frequencies with increasing the age of conservation. It has been proved that hydration reactions occur continuously during the curing period. The absorption peak of Si(Al)-O-Si in the figure shifts about 17 cm^{-1} toward the high frequency, probably due to the substitution of Cr for Si or Al into the tetrahedra to get solidified, affecting the structural ordering, which combined with XRD proves the involvement of heavy metal Cr in the reaction to generate calcium-chromium garnet.

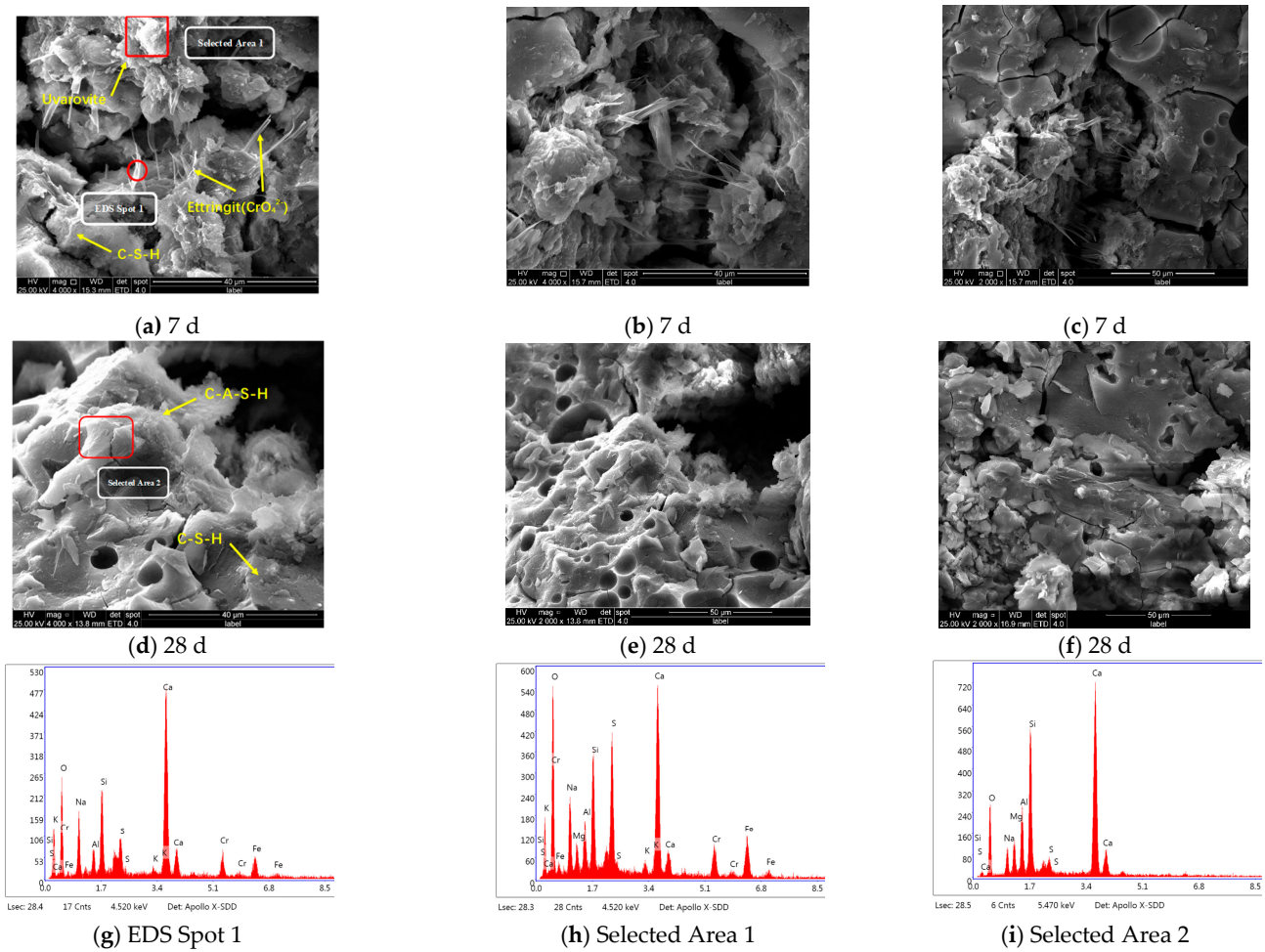


Figure 10. SEM images and EDS spectra of the ATSSP with the optimal mix ratio.

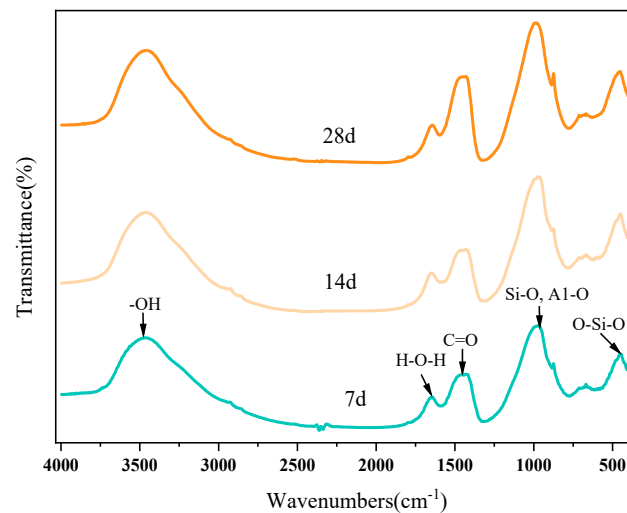


Figure 11. FT-IR spectrum of ATSSG at different ages.

4. Conclusions

In this study, based on the RSM, an alkali-excited tannery sludge–slag curing body was prepared with tannery sludge and slag as materials, and the compressive strength characteristics and the curing effect on heavy metal Cr were investigated by multiscale tests. The main conclusions are as follows:

(1) The single-factor test verification showed that the alkali-excited tannery sludge–slag curing body has high early strength, and the 7 d average compressive strength can reach approximately 45 MPa. The three factors activator–binder ratio, alkali-activation modulus, and water–binder ratio have a large influence and a more significant regular relationship with the compressive strength of this material.

(2) By RSM test, a quadratic multiple regression model of 7 d and 28 d compressive strength of alkali-excited tannery sludge–slag curing body was established based on the three factors of activator–binder ratio, alkali-activation modulus, and water–binder ratio. Based on the model, the best ratio of alkali-excited tannery sludge–slag curing body is obtained by numerical optimization: The activator–binder ratio is approximately 21.74%, the modulus of excitation is approximately 1.02, and the water–binder ratio is 0.37. The ratio of 0.37 is the best. At this time, the measured 28 d compressive strength can reach 71.3 MP, and the relative error between the measured value and the predicted value (70.71 MPa) is only 0.82%, which is less than 1%. This study provides a reference for the design of alkali-excited cementitious material system ratios with important reference values and guidance significance.

(3) Based on microscopic analysis, the hydration mechanism of the alkali-excited tannery sludge–slag curing body and its mechanism of curing heavy metals were investigated. On the one hand, the main hydration products of the material are hydrated calcium silicate (C-S-H) and calcite (CaCO_3), which form a dense cage-like three-dimensional mesh structure, which ensures its excellent mechanical properties and good wrapping and adsorption of tannery sludge Cr (III). On the other hand, the material can also rely on slag-reducing components (Fe^{2+} , S^{2-}) to reduce part of Cr (VI) to Cr (III) and adsorb solid solution or form calcium-chromium garnet ($\text{Ca}_3\text{Cr}_2[\text{SiO}_4]_3$), while the unreduced Cr (VI) is mainly physically sequestered by the cage-like three-dimensional mesh structure of hydration products, achieving the effect of solidifying Cr.

(4) Under the optimal mix ratio, the total Cr and Cr (VI) precipitation concentration and leaching rate of the material are 1 mg/L and 1.27%, 0.05 mg/L and 15.77%, respectively, which meet the specification requirements. This provides important support for the utilization of building materials from tannery sludge.

The experimental results indicate that the blending of slag and tannery sludge can yield an eco-friendly cementitious material, with the product exhibiting superior mechanical properties and the ability to immobilize heavy metals. Based on the findings and observations, it is recommended to conduct further durability studies (such as thermostability and acid and alkali resistance) using these materials (slag and tannery sludge). This is to understand the behavior of slag and tannery sludge-based polymers when exposed to chemical environments and their resistance to adverse environmental conditions. Simultaneously, the concentration of Cr release and leaching rate of ATSSP should be monitored during this process. The understanding of the form and valence changes of heavy metal Cr during durability testing will provide further support for the harmless and construction material utilization of tannery sludge.

Author Contributions: Software, M.Z.; Validation, H.S.; Data curation, Y.B.; Writing—original draft, P.D.; Writing—review & editing, S.C. All authors have read and agreed to the published version of the manuscript.

Funding: This work was supported by the North China University of Water Resources and Electric Power. The authors also would like to acknowledge the support of the National Natural Science Foundation of China (52009045), the National Natural Science Foundation of China (51979169), and the Henan Science and Technology Project (212102310539).

Data Availability Statement: Data will be made available on request.

Conflicts of Interest: The authors declare that they have no known competing financial interests or personal relationships that could have appeared to influence the work reported in this paper.

References

1. Merlet, Y.; Rouchier, S.; Jay, A.; Cellier, N.; Woloszyn, M. Integration of phasing on multi-objective optimization of building stock energy retrofit. *Energy Build.* **2022**, *257*, 111776. [[CrossRef](#)]
2. Zhou, Y.; Li, W.; Peng, Y.; Tang, S.; Wang, L.; Shi, Y.; Wu, K. Hydration and fractal analysis on low-heat portland cement pastes using thermodynamics-based methods. *Fractal Fract.* **2023**, *7*, 606. [[CrossRef](#)]
3. Wani, O.B.; Khan, S.; Shoaib, M.; Zeng, H.; Bobicki, E.R. Decarbonization of mineral processing operations: Realizing the potential of carbon capture and utilization in the processing of ultramafic nickel ores. *Chem. Eng. J.* **2022**, *433*, 134203. [[CrossRef](#)]
4. Sruthi, S.; Gayathri, V. Synthesis and Evaluation of Eco-Friendly, Ambient-Cured, Geopolymer-Based Bricks Using Industrial By-Products. *Buildings* **2023**, *13*, 510. [[CrossRef](#)]
5. Zeraoui, A.; Maherzi, W.; Benzerzour, M.; Abriak, N.E.; Aouad, G. Development of Flash-Calcined Sediment and Blast Furnace Slag Ternary Binders. *Buildings* **2023**, *13*, 333. [[CrossRef](#)]
6. Fan, L.F.; Chen, D.K.; Zhong, W.L. Effects of slag and alkaline solution contents on bonding strength of geopolymer-concrete composites. *Constr. Build. Mater.* **2023**, *406*, 133391. [[CrossRef](#)]
7. Ma, H.; Zhou, J.; Hua, L.; Cheng, F.; Zhou, L.; Qiao, X. Chromium recovery from tannery sludge by bioleaching and its reuse in tanning process. *J. Clean. Prod.* **2017**, *142*, 2752–2760. [[CrossRef](#)]
8. Nighot, N.S.; Kumar, R.A. comprehensive study on the synthesis and characterization of eco-cementitious binders using different kind of industrial wastes for sustainable development. *Dev. Built Environ.* **2023**, *14*, 100135. [[CrossRef](#)]
9. Juel, M.A.I.; Alam, M.S.; Pichtel, J.; Ahmed, T. Environmental and health risks of metal-contaminated soil in the former tannery area of Hazaribagh, Dhaka. *SN Appl. Sci.* **2020**, *2*, 1915.
10. Mpofo, A.B.; Oyekola, O.O.; Welz, P.J. Co-digestion of tannery waste activated sludge with slaughterhouse sludge to improve organic biodegradability and biomethane generation. *Process Saf. Environ. Prot.* **2019**, *131*, 235–245. [[CrossRef](#)]
11. Basegio, T.; Berutti, F.; Bernardes, A.; Bergmann, C.P. Environmental and technical aspects of the utilisation of tannery sludge as a raw material for clay products. *J. Eur. Ceram. Soc.* **2002**, *22*, 2251–2259. [[CrossRef](#)]
12. Filibeli, A.; Buyukkamaci, N.; Senol, H. Solidification of tannery wastes. *Resour. Conserv. Recycl.* **2000**, *29*, 251–261. [[CrossRef](#)]
13. Jin, M.; Lian, F.; Xia, R.; Wang, Z. Formulation and durability of a geopolymer based on metakaolin/tannery sludge. *Waste Manag.* **2018**, *79*, 717–728. [[CrossRef](#)]
14. Amin, S.K.; Ashmawy, N.M.F.; Abadir, M.F. The use of tannery waste in the preparation of clay roof tiles. *Constr. Build. Mater.* **2022**, *325*, 126393. [[CrossRef](#)]
15. Ivanov, R.C.; da Luz, C.A.; Zorel, H.E., Jr.; Pereira Filho, J.I. Behavior of calcium aluminate cement (CAC) in the presence of hexavalent chromium. *Cem. Concr. Compos.* **2016**, *73*, 114–122. [[CrossRef](#)]
16. Jin, M.; Wang, Z.; Lian, F.; Zhao, P. Freeze-thaw resistance and seawater corrosion resistance of optimized tannery sludge/metakaolin-based geopolymer. *Constr. Build. Mater.* **2020**, *265*, 120730. [[CrossRef](#)]
17. Prasittisopin, L.; Trejo, D. Performance characteristics of blended cementitious systems incorporating chemically transformed rice husk Ash. *Adv. Civ. Eng. Mater.* **2017**, *6*, 17–35. [[CrossRef](#)]
18. Prasittisopin, L.; Trejo, D. Effects of mixing time and revolution count on characteristics of blended cement containing rice husk ash. *J. Mater. Civ. Eng.* **2018**, *30*, 04017262. [[CrossRef](#)]
19. Odimegwu, T.C.; Kaish, A.B.M.A.; Jamil, M.; Zain, M.F.M.; Turlanbekov, A.; Al Zand, A.W. Mechanical Characterization of Geopolymer Paste and Mortar Fabricated from Alum Sludge and Fly Ash. *Buildings* **2023**, *13*, 2118. [[CrossRef](#)]
20. Huang, G.; Yang, K.; Sun, Y.; Lu, Z.; Zhang, X.; Zuo, L.; Xu, Z. Influence of NaOH content on the alkali conversion mechanism in MSWI bottom ash alkali-activated mortars. *Constr. Build. Mater.* **2020**, *248*, 118582. [[CrossRef](#)]
21. Luhar, I.; Luhar, S.; Abdullah, M.M.A.B.; Razak, R.A.; Vizureanu, P.; Sandu, A.V.; Matasar, P.D. A state-of-the-art review on innovative geopolymer composites designed for water and wastewater treatment. *Materials* **2021**, *14*, 7456. [[CrossRef](#)]
22. Sandanayake, M.; Gunasekara, C.; Law, D.; Zhang, G.; Setunge, S.; Wanijuru, D. Sustainable criterion selection framework for green building materials—An optimisation based study of fly-ash Geopolymer concrete. *Sustain. Mater. Technol.* **2020**, *25*, e00178. [[CrossRef](#)]
23. He, P.; Zhang, Y.; Zhang, X.; Chen, H. Diverse zeolites derived from a circulating fluidized bed fly ash based geopolymer for the adsorption of lead ions from wastewater. *J. Clean. Prod.* **2021**, *312*, 127769. [[CrossRef](#)]
24. Chen, X.; Guo, Y.; Ding, S.; Zhang, H.; Xia, F.; Wang, J.; Zhou, M. Utilization of red mud in geopolymer-based pervious concrete with function of adsorption of heavy metal ions. *J. Clean. Prod.* **2019**, *207*, 789–800. [[CrossRef](#)]
25. El-Eswed, B.I.; Yousef, R.I.; Alshaaer, M.; Hamadneh, I.; Al-Gharabli, S.I.; Khalili, F. Stabilization/solidification of heavy metals in kaolin/zeolite based geopolymers. *Int. J. Miner. Process.* **2015**, *137*, 34–42. [[CrossRef](#)]
26. Nikolić, V.; Komljenović, M.; Džunuzović, N.; Ivanović, T.; Miladinović, Z. Immobilization of hexavalent chromium by fly ash-based geopolymers. *Compos. Part B Eng.* **2017**, *112*, 213–223. [[CrossRef](#)]
27. Zhao, Q.; Yang, B.; Ren, H.; Chen, S.; Luo, C.; Li, Q.; Yan, K. Removal of Cr (VI) from aqueous systems using FeP slag as a reducing agent. *Hydrometallurgy* **2022**, *211*, 105875. [[CrossRef](#)]
28. Galiano, Y.L.; Pereira, C.F.; Vale, J. Stabilization/solidification of a municipal solid waste incineration residue using fly ash-based geopolymers. *J. Hazard. Mater.* **2011**, *185*, 373–381. [[CrossRef](#)]
29. Ye, H.; Chen, Z.; Huang, L. Mechanism of sulfate attack on alkali-activated slag: The role of activator composition. *Cem. Concr. Res.* **2019**, *125*, 105868. [[CrossRef](#)]

30. Azmakan, A.; Ahmadi, J.; Shahani, A.; Badarloo, B.; Garbowski, T. Optimal Quantity Investigation of Metakaolin and Silica Fume in Production of Durable Acid Resistance Alkali Activated Slag Concrete. *Buildings* **2023**, *14*, 21. [[CrossRef](#)]
31. Jiang, D.; Shi, C.; Zhang, Z. Recent progress in understanding setting and hardening of alkali-activated slag (AAS) materials. *Cem. Concr. Compos.* **2022**, *134*, 104795. [[CrossRef](#)]
32. San Nicolas, R.; Provis, J.L. The interfacial transition zone in alkali-activated slag mortars. *Front. Mater.* **2015**, *2*, 70. [[CrossRef](#)]
33. Chen, S.; Lu, P.; Bie, Y.; Wang, L.; Guo, L. Mechanical properties and micro mechanism of alkali-activated tannery sludge/fly ash composite cement-based recycled concrete. *Constr. Build. Mater.* **2023**, *391*, 131813. [[CrossRef](#)]
34. Chen, S.; Liu, Y.; Bie, Y.; Duan, P.; Wang, L. Multi-scale performance study of concrete with recycled aggregate from tannery sludge. *Case Stud. Constr. Mater.* **2022**, *17*, e01698. [[CrossRef](#)]
35. GB/T 18046-2017; Ground Granulated Blast Furnace Slag Used for Cement, Mortar and Concrete. China Building Materials Federation: Beijing, China, 2017.
36. Ding, G.; Xu, J.; Wei, Y.; Chen, R.; Li, X. Engineered reclamation fill material created from excavated soft material and granulated blast furnace slag. *Resour. Conserv. Recycl.* **2019**, *150*, 150. [[CrossRef](#)]
37. Chaouche, M.; Gao, X.X.; Cyr, M.; Cotte, M.; Frouin, L. On the origin of the blue/green color of blast-furnace slag-based materials: Sulfur K-edge XANES investigation. *J. Am. Ceram. Soc.* **2018**, *100*, 1707–1716. [[CrossRef](#)]
38. Huang, J.; Li, W.; Huang, D.; Wang, L.; Chen, E.; Wu, C.; Li, Y. Fractal analysis on pore structure and hydration of magnesium oxysulfate cements by first principle, thermodynamic and microstructure-based methods. *Fractal Fract.* **2021**, *5*, 164–181. [[CrossRef](#)]
39. Peng, Y.; Tang, S.; Huang, J.; Tang, C.; Wang, L.; Liu, Y. Fractal analysis on pore structure and modeling of hydration of magnesium phosphate cement paste. *Fractal Fract.* **2022**, *6*, 337–355. [[CrossRef](#)]
40. Tang, S.; Wang, Y.; Geng, Z.; Xu, X.; Yu, W.; Chen, J. Structure, fractality, mechanics and durability of calcium silicate hydrates. *Fractal Fract.* **2021**, *5*, 47–80. [[CrossRef](#)]
41. HJ/T 299-2007; Solid Waste-Extraction Procedure for Leaching Toxicity. Sulphuric Acid & Nitric Acid Method. Ministry of Ecology and Environment of People's Republic of China: Beijing, China, 2007.
42. GB/T 15555.4-1995; Solid Waste-Determination of Chromium (VI)-1,5-Diphenylcarbohydrazide Spectrophotometric Method. Ministry of Ecology and Environment of People's Republic of China: Beijing, China, 1995.
43. Zhang, Q.; Feng, X.; Chen, X.; Lu, K. Mix design for recycled aggregate pervious concrete based on response surface methodology. *Constr. Build. Mater.* **2020**, *259*, 119776. [[CrossRef](#)]
44. Pacheco-Torgal, F.; Castro-Gomes, J.; Jalali, S. Alkali-activated binders: A review Part 1. Historical background, terminology, reaction mechanisms and hydration products. *Constr. Build. Mater.* **2008**, *22*, 1305–1314. [[CrossRef](#)]
45. GB 5085.3-1996; Identification Standards for Hazardous Wastes-Identification for Extraction Toxicity. Ministry of Ecology and Environment of People's Republic of China: Beijing, China, 1996.
46. Zhang, M.; Yang, C.; Zhao, M.; Yang, K.; Shen, R.; Zheng, Y. Immobilization potential of Cr (VI) in sodium hydroxide activated slag pastes. *J. Hazard. Mater.* **2017**, *321*, 281–289. [[CrossRef](#)] [[PubMed](#)]
47. Dong, P.; Ding, W.; Yuan, H.; Wang, Q. 3D-printed polymeric lattice-enhanced sustainable municipal solid waste incineration fly ash alkali-activated cementitious composites. *Dev. Built Environ.* **2022**, *12*, 100101. [[CrossRef](#)]
48. Bahmani, H.; Mostofinejad, D. A review of engineering properties of ultra-high-performance geopolymer concrete. *Dev. Built Environ.* **2023**, *14*, 100126. [[CrossRef](#)]
49. Deja, J. Immobilization of Cr⁶⁺, Cd²⁺, Zn²⁺ and Pb²⁺ in alkali-activated slag binders. *Cem. Concr. Res.* **2002**, *32*, 1971–1979. [[CrossRef](#)]
50. Kaze, C.R.; à Mounsam, L.M.B.; Metekong, J.V.S.; Alomayri, T.S.; Naghizadeh, A.; Tchadjie, L. Thermal behaviour, microstructural changes and mechanical properties of alkali-activated volcanic scoria-fired waste clay brick blends. *Dev. Built Environ.* **2023**, *14*, 100153. [[CrossRef](#)]
51. Li, N.; Farzadnia, N.; Shi, C. Microstructural changes in alkali-activated slag mortars induced by accelerated carbonation. *Cem. Concr. Res.* **2017**, *100*, 214–226. [[CrossRef](#)]

Disclaimer/Publisher's Note: The statements, opinions and data contained in all publications are solely those of the individual author(s) and contributor(s) and not of MDPI and/or the editor(s). MDPI and/or the editor(s) disclaim responsibility for any injury to people or property resulting from any ideas, methods, instructions or products referred to in the content.